CrystEngComm

ROYAL SOCIETY OF CHEMISTRY

PAPER

Cite this: *CrystEngComm*, 2020, **22**, 1197

Double-shell SnO_2@Fe_2O_3 hollow spheres as a high-performance anode material for lithium-ion batteries

Zhipeng Cui, Meng Sun, Huanqing Liu, Sijie Li, Qingye Zhang, Chengpeng Yang, Guiju Liu, Junyu Zhong* and Yiqian Wang *

Received 14th October 2019,
Accepted 2nd January 2020

DOI: 10.1039/c9ce01621j

rsc.li/crystengcomm

Construction of novel electrode materials is an effective way to enhance the electrochemical performance of lithium ion batteries (LIBs). In this work, double-shell SnO_2@Fe_2O_3 hollow spheres are fabricated through a simple template method. It is revealed that the α-Fe_2O_3 nanorods are heterogeneously assembled on the surfaces of hollow SnO_2 spheres. The double-shell SnO_2@Fe_2O_3 hollow spheres, as an anode material for LIBs, demonstrate excellent lithium storage capacity and cycling stability. Their discharge specific capacity decreases to 464 mA h g^{-1} for the 46th cycle at a current density of 100 mA g^{-1}, and then increases significantly to 1043 mA h g^{-1} up to the 190th cycle. Compared with SiO_2@SnO_2 (221 mA h g^{-1} after 190 cycles) and SnO_2 (336 mA h g^{-1} after 190 cycles) electrodes, the better electrochemical performance of the SnO_2@Fe_2O_3 electrode is ascribed to its hierarchical hollow urchin-like structure, the SnO_2@Fe_2O_3 heterojunctions and the oxygen vacancies in the α-Fe_2O_3 nanorods. The sea urchin-like heterostructures dramatically inhibit the agglomeration and prevent the volume expansion during the cycling process. This work provides a novel way to construct a promising material with enhanced performance as an anode for LIBs.

1. Introduction

With the emergence of electric cars and portable electronic products, there is a fast growing need for clean and sustainable energy storage. Lithium ion batteries (LIBs) are widely used for effective energy storage because of their high power density, high energy density and long cycle life.[1–4] Nowadays, as a universal anode material for commercial LIBs, graphite limits the development for high performance LIBs, as it suffers from a low theoretical capacity (372 mA h g^{-1}).[5,6] To increase the specific capacity of batteries, much effort is devoted to the development of new anode materials for LIBs, especially metallic oxides with high specific capacity.

As common n-type semiconductor materials, tin oxide (SnO_2) and hematite (Fe_2O_3) have attracted considerable attention due to their high theoretical specific capacities (781 mA h g^{-1} for SnO_2 and 1007 mA h g^{-1} for Fe_2O_3) and environmental friendliness.[7,8] Nevertheless, there are still some restrictions on their applications in LIBs, such as significant agglomeration and volume expansion (about 300% for SnO_2) caused by Li^+ insertion/extraction. These problems result in severe pulverization of electrode active materials, eventually leading to a rapid decrease of specific capacity and poor cycling stability.

To improve the cycling stability of SnO_2 and Fe_2O_3, various nanostructures have been proposed, such as nanoribbons,[9] nanorods,[10] hollow nanoplates,[11] hollow nanospheres,[12] and nanospindles.[13] These nanostructures can alleviate volume expansion and shorten the channel of electron transport between the electrode and electrolyte. In particular, the hollow sphere structure is the one that possesses great advantages due to its high specific surface area, short diffusion length for lithium and improved cycling stability.

Apart from various unique nanostructures, fabricating SnO_2@Fe_2O_3 composite structures is another effective way to improve the cycling stability, by benefiting from the synergistic effect of the two materials, and inhibitory effect on agglomeration and volume expansion problems of individual components. Several multi-layered SnO_2@Fe_2O_3 nanocomposites with different morphologies have been prepared by various synthesis routes. For example, Yan *et al.*[14] prepared SnO_2–Fe_2O_3 nanocubes using a solvothermal method, which exhibit a reversible capacity of 567.5 mA h g^{-1} after 50 cycles at 200 mA g^{-1}. Zeng *et al.*[15] reported SnO_2@Fe_2O_3 sandwich nanocubes by compositing Fe_2O_3 nanorods with SnO_2 nanocubes, showing a reversible capacity of 750.8 mA h g^{-1} after 200 cycles at 500 mA g^{-1}. Jin *et al.*[16] fabricated hierarchical SnO_2/Fe_2O_3 hollow spheres *via* a

College of Physics & State Key Laboratory of Bio-Fibers and Eco-Textiles, Qingdao University, No. 308 Ningxia Road, Qingdao, 266071, People's Republic of China. E-mail: jyzhong@qdu.edu.cn, yqwang@qdu.edu.cn; Tel: +86 532 83780318

solvothermal method, which demonstrate a high capacity and good rate performance. Furthermore, Choi *et al.*[17] synthesized SnO_2–Fe_2O_3–C hollow spheres though a template-based sol–gel method and hydrothermal method, which present a reversible capacity of 1100 mA h g^{-1} after 100 cycles at 200 mA g^{-1}. The outer carbon layer plays an important role in improving the electrochemical performance, such as enhancing the electrical conductivity and preventing large volume change during the cycling process. However, it is still a great challenge to synthesize uniform hollow urchin-like heterostructures with superior cycling performance and keep their original structure after repeated Li^+ insertion/extraction. A few reports have been found to explore the effect of the heterojunction interface on the specific capacity and cycling stability.

In our work, we combined a template method with a hydrothermal method to prepare urchin-like SnO_2@α-Fe_2O_3 hollow spheres, which has an advantage to control the size of the hollow spheres more uniformly. Compared with SiO_2@SnO_2 and SnO_2 hollow spheres, the urchin-like SnO_2@α-Fe_2O_3 hollow sphere electrode exhibits enhanced reversible capacity and better cycling performance. The improved electrochemical performance is attributed to the stability of the urchin-like heterostructures, oxygen vacancies in the Fe_2O_3 nanorods and the heterojunction interface between the SnO_2 hollow nanospheres and α-Fe_2O_3 nanorods.

2. Experimental section

2.1. Synthesis of SnO_2 hollow spheres

The monodisperse SiO_2 spheres were produced using a modified Stöber method.[18] At first, 2 mL tetraethyl orthosilicate was dissolved in a mixture of 75 mL methanol, 10 mL deionized (DI) water and 8 mL ammonia water. The mixture reacted at room temperature for 3 h. White products were collected by centrifugation, washed several times with DI water and ethanol, and dried at 60 °C for 12 h. Afterward, 10 mmol of SiO_2 synthesized powder was dispersed in 50 mL DI water. 10 mmol $Na_2SnO_3{\cdot}4H_2O$ was added into a mixing solution of 50 mL ethanol and 50 mL DI water, and then it was added to the suspension of SiO_2 spheres and stirred vigorously at 60 °C for 3 h. The white precipitates were separated by centrifugation, washed with DI water and ethanol, and dried at 80 °C overnight, followed by calcination at 600 °C for 1 h. The synthesized SnO_2-coated SiO_2 spheres (hereafter called SiO_2@SnO_2) were dispersed in 2 M NaOH solution and reacted for 1.5 h at 50 °C. The SnO_2 hollow spheres were obtained by centrifugation and dried at 80 °C.

2.2. Synthesis of double-shell SnO_2@Fe_2O_3 hollow spheres

0.33 mmol SnO_2 powder was dispersed in DI water and stirred vigorously. Afterwards 0.8 mmol $FeCl_3{\cdot}6H_2O$ and 0.8 mmol Na_2SO_4 were dispersed in the SnO_2 suspension. Subsequently, the resulting solution was transferred into a Teflon-sealed autoclave and heated at 120 °C for 8.5 h. After calcining at 500 °C for 2 h in air, the hollow SnO_2@Fe_2O_3 spheres with double shells were obtained.

2.3. Materials characterization

The crystal structures were analyzed by X-ray diffraction (XRD) using a SmartLab X-ray diffractometer with Cu Kα radiation (λ = 1.5406 Å). The morphology was characterized using a field-emission scanning electron microscope (FESEM, Hitachi S-4800) at an acceleration voltage of 15 kV. Bright-field (BF) and high-resolution transmission electron microscopy (HRTEM) images and selected-area electron diffraction (SAED) patterns were obtained using a JEOL JEM 2100F transmission electron microscope (TEM) operated at 200 kV. The elemental mapping images were obtained on an FEI Tecnai G2 F20 TEM. X-ray photoelectron spectroscopy (XPS) was carried out on a Thermo ESCALAB 250XI. Nitrogen adsorption–desorption tests were carried out using an automatic volumetric sorption analyzer (NOVA 1100, Quantachrome, USA) at 77 K. Scanning-transmission electron microscopy (STEM) images and electron energy-loss spectroscopy (EELS) spectra were obtained on a JEM ARM200CF transmission electron microscope operated at 200 kV.

2.4. Electrochemical measurements

We assembled CR2025-type coin cells in a high-purity argon-filled glove box, where the moisture and oxygen concentration is less than 0.1 ppm, using lithium foil as the counter electrode. The anodes were prepared by mixing the active material (SiO_2@SnO_2 spheres, SnO_2 hollow spheres or double-shell SnO_2@Fe_2O_3 hollow spheres), carbon black and water-soluble sodium alginate (SA) in a weight ratio of 70 : 15 : 15 (wt%) onto pure copper foil. The loading density of the three samples (SiO_2@SnO_2 powder, SnO_2 hollow spheres and SnO_2@Fe_2O_3 hollow spheres) was 0.51 mg cm^{-2}. The electrolyte was a mixture of 1 M $LiPF_6$ solution and ethylene carbonate (EC)/diethyl carbonate (DEC)/dimethyl carbonate (DMC) (1 : 1 : 1 in volume). The cycle and rate performances were characterized using a LAND CT2001 battery test system in a voltage range from 0.01 V to 3.00 V. Cyclic voltammetry (CV) tests were performed on a Metrohm Autolab electrochemical workstation (PGSTAT 302N) between 0.01 V and 3.00 V with a scan rate of 0.1 mV s^{-1}. Electrochemical impedance spectroscopy (EIS) measurements were carried out on a Metrohm Autolab electrochemical workstation (PGSTAT 302N) under open-circuit voltage. The EIS tests were carried out at a frequency range from 100 kHz to 0.01 Hz with a disturbance amplitude of 5 mV.

3. Results and discussion

Fig. 1 shows the XRD patterns of the SiO_2, SnO_2 hollow spheres and double-shell SnO_2@Fe_2O_3 hollow spheres. All the diffraction peaks of the SnO_2 hollow spheres are consistent with tetragonal rutile SnO_2 (JCPDS no.: 41-1445), and no SiO_2

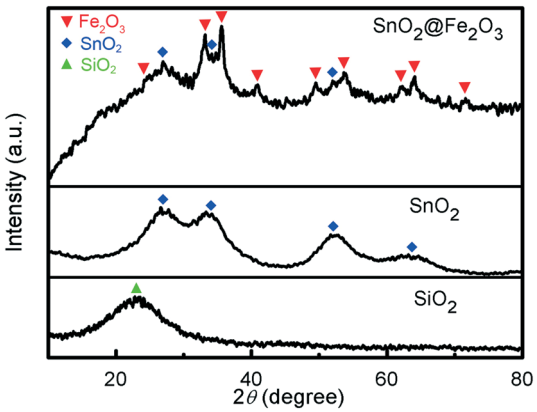

Fig. 1 XRD patterns of the SiO_2, SnO_2 and double-shell SnO_2@Fe_2O_3 hollow spheres.

signal is visible, which suggests that the SiO_2 template has been removed completely. Due to the small size of particles, the peaks of SnO_2 are broadened. The XRD patterns of the SnO_2@Fe_2O_3 hollow spheres are a good match to those of the tetragonal rutile structure of SnO_2 (JCPDS no.: 41-1445, $a = b = 0.4738$ nm, $c = 0.3187$ nm) and rhombohedral structure of α-Fe_2O_3 (JCPDS no.: 33-0664, $a = b = 0.5035$ nm, $c = 1.375$ nm), respectively. Thin SnO_2 peaks are observed, as if some larger SnO_2 crystalline structures are present in this material. No peaks from other impurities are observed, indicating that the SnO_2@Fe_2O_3 hollow spheres are of high purity.

XPS analyses were carried out to further investigate the chemical composition of the double-shell SnO_2@Fe_2O_3 hollow spheres. The C 1s peak is located at 284.8 eV (Fig. 2a), indicating the emergence of surface adventitious carbon. The other binding energies were calibrated by the C 1s peak. Fig. 2b shows that the O 1s spectrum is divided into three peaks at 530.3 eV, 531.6 eV and 532.7 eV, corresponding to the O^{2-}, OH^- and H_2O molecules, respectively.[19] As shown in Fig. 2c, the $3d_{5/2}$ and $3d_{3/2}$ binding energies of the Sn peaks are located at 486.9 eV and 495.3 eV, respectively, separated by an energy of 8.4 eV, which can be ascribed to the 3d binding energy of Sn^{4+}–O.[17] In Fig. 2d, the spectrum is fitted into three single peaks at 711.1 eV, 713.7 eV and 716.7 eV, which are associated with Fe^{3+} $2p_{3/2}$, Fe^{2+} $2p_{3/2}$ and Sn $3p_{3/2}$, respectively.[17] It can be found that there is a small amount of Fe^{2+} in the as-prepared sample, which is attributed to the presence of oxygen vacancies. Hence, the XPS examinations show that the sample is composed of SnO_2 and Fe_2O_3 with a small amount of oxygen vacancies.

The morphologies and structures of the SnO_2 hollow spheres were characterized by FESEM and TEM, as shown in Fig. 3. Fig. 3a shows the typical FESEM image of the hollow SnO_2 spheres with a size of 270 ± 10 nm. In addition, some broken spheres can also be observed. Careful examination

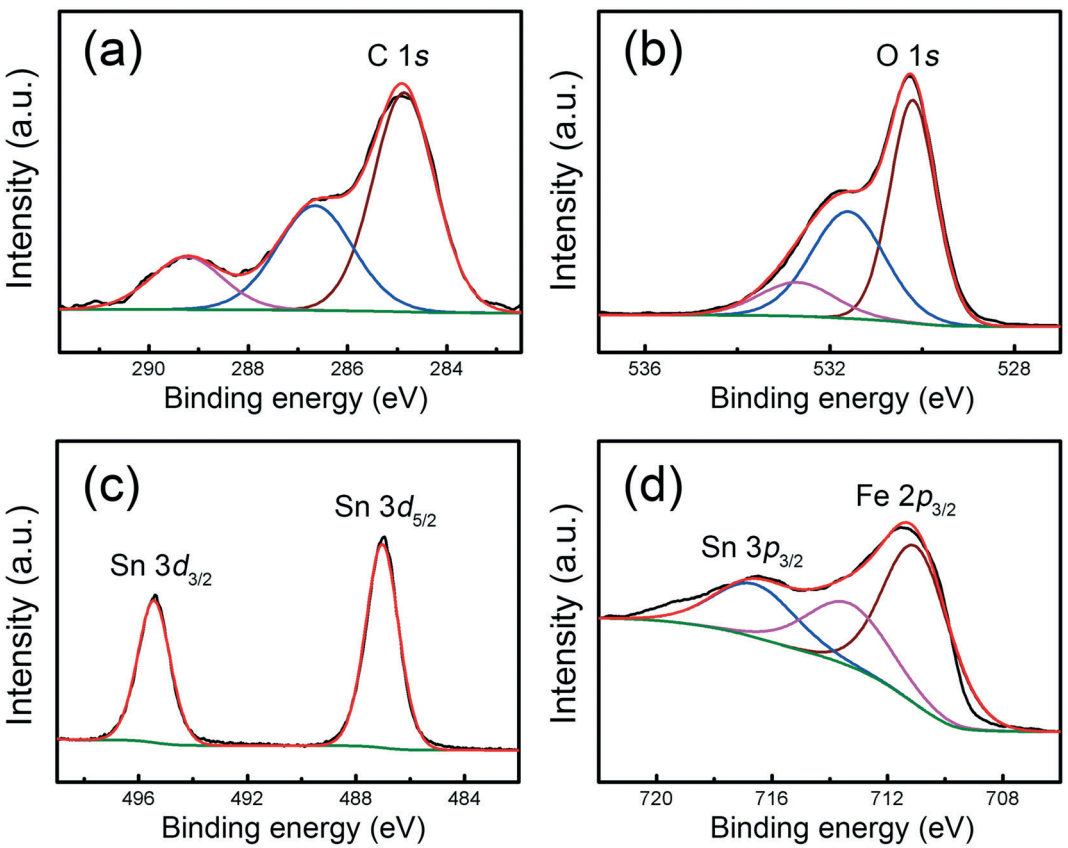

Fig. 2 (a) C 1s, (b) O 1s, (c) Sn 3d and (d) Fe 2p XPS spectra of the double-shell SnO_2@Fe_2O_3 hollow spheres.

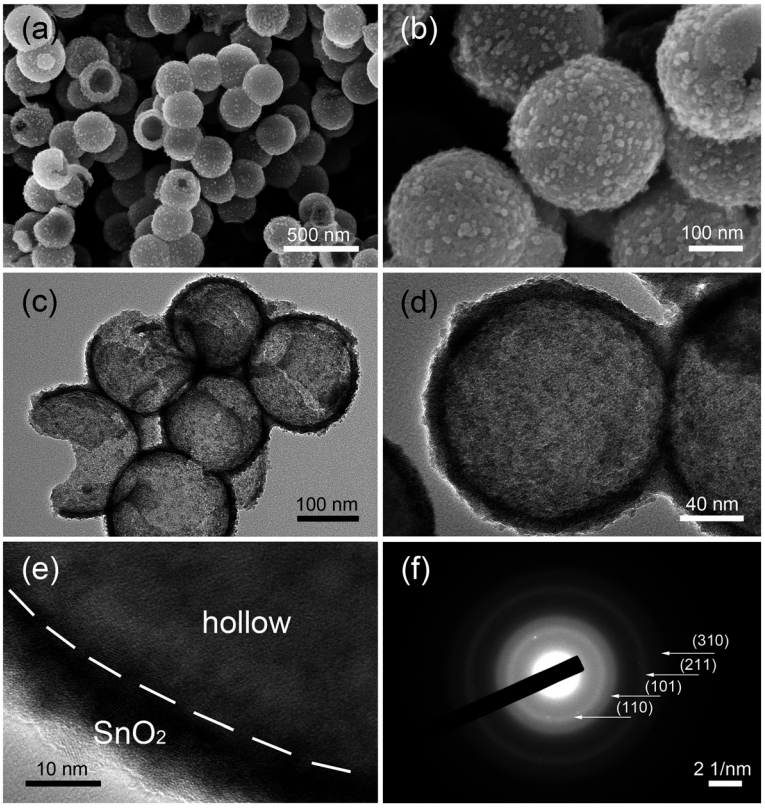

Fig. 3 Low-magnification (a) and high-magnification (b) FESEM images of the SnO_2 spheres. Typical BF TEM image (c) and enlarged TEM image (d) of the SnO_2 spheres. (e) Typical HRTEM image of the SnO_2 spheres. (f) SAED patterns obtained from the SnO_2 spheres.

shows that the sphere surfaces are covered with many small dots. To see the surface morphology of the SnO_2 hollow spheres more clearly, an enlarged FESEM image is presented in Fig. 3b. It is found that the SnO_2 hollow spheres are self-assembled from many primary nanoparticles, the largest of which have about 13.5 nm. To obtain more detailed microstructure information about the spheres, extensive TEM was carried out. Fig. 3c shows the typical TEM image of the SnO_2 hollow spheres. It can be seen that the contrast of the shell is darker than that of the interior, proving that the interior is hollow. Fig. 3d shows the magnified TEM image, from which it can be seen that the SnO_2 shell has a thickness of about 15 nm. The boundary between the hollow interior and the outer SnO_2 shell is marked in Fig. 3e. The SAED patterns (Fig. 3f) can be indexed to tetragonal rutile SnO_2, consistent with the XRD results. Four diffraction rings from the center to the outside correspond to the (110), (101), (211) and (310) planes of SnO_2, which demonstrates the polycrystalline nature of the SnO_2 hollow spheres.

To analyze the chemical composition of the SnO_2 hollow spheres, EELS was carried out. Fig. 4a shows the typical STEM image of the SnO_2 hollow spheres. The size of the hollow spheres is measured to be 270 ± 10 nm, consistent with the FESEM results. Fig. 4b presents an enlarged image of an individual hollow sphere. It can clearly be seen that the contrast of the shell is brighter than that of the interior, which is the inverse of what was observed in the TEM image. Since the contrast of STEM image is proportional to the square of the atomic number (Z) of elements, this further proves that the SnO_2 spheres are hollow. Fig. 4c and d show the EELS spectra of Sn $M_{4,5}$-edge and O K-edge. According to the relative position of the Sn $M_{4,5}$-edge peaks, valence states of Sn can be inferred.[20,21] It is reported that for SnO_2, the separation between M_5 edge and the first oxygen peak is a significant feature.[20] The EELS spectra are calibrated by the first oxygen peak situated at 532 eV. The Sn M_5 edge is located at 490 eV and the spacing between Sn M_5 and M_4 edges is 8.2 eV, as shown in Fig. 4c. In Fig. 4d, the two peaks of O K-edge, labeled A and B, have an energy spacing of 6 eV, demonstrating that Sn has an oxidation state of 4+, consistent with our XPS measurement and previous work.[20] Thus, the composition of the shells in the hollow spheres is determined to be SnO_2.

To observe the morphologies and internal structure of the as-prepared SnO_2@α-Fe_2O_3 hollow spheres, FESEM and TEM were carried out. As can be seen from the FESEM images in Fig. 5a and b, the SnO_2@α-Fe_2O_3 hollow spheres look like sea urchins with an average diameter of about 340 nm. From the TEM image in Fig. 5c, it can be seen that the composite possesses a hollow hierarchical structure. In addition, the α-Fe_2O_3 nanorods with a length of about 35 nm are heterogeneously assembled on the surface of the hollow SnO_2 spheres. The enlarged TEM image in Fig. 5d shows a single SnO_2@α-Fe_2O_3 hollow sphere. It is apparent that the

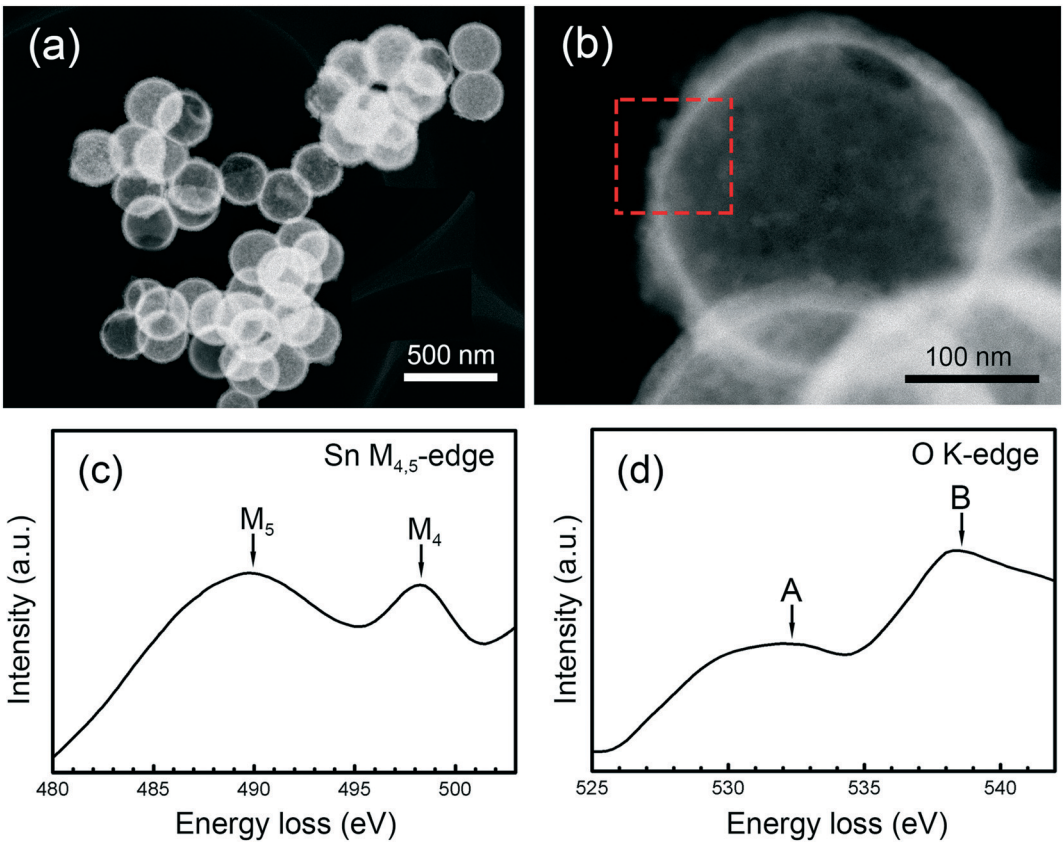

Fig. 4 Typical STEM image (a) and an enlarged STEM image (b) of the SnO_2 spheres. EELS spectra of Sn $M_{4,5}$-edge (c) and O K-edge (d) obtained from the SnO_2 spheres.

sphere possesses a hollow structure with inner and outer shells. Through examining the contrast of the TEM image, the inner shell corresponds to SnO_2 and the outer shell is composed of α-Fe_2O_3 nanorods. Some nanopores are marked by red circles in Fig. 5d, which could facilitate full contact with the electrolyte in the LIBs. Fig. 5e presents the elemental mapping images of a single SnO_2@Fe_2O_3 hollow sphere. The spatial distributions of Sn, Fe and O elements prove that the Fe_2O_3 nanorods are coated on the SnO_2 hollow spheres.

To obtain more detailed crystal structure information on the α-Fe_2O_3 nanorods, TEM was carried out. Fig. 6a shows the typical BF TEM image of the SnO_2@α-Fe_2O_3 spheres. It can be seen that numerous α-Fe_2O_3 nanorods grow on the hollow spheres. Fig. 6b presents an enlarged HRTEM image of the region enclosed by a red rectangle in Fig. 6a. It clearly shows that the α-Fe_2O_3 nanorod grows along the $[10\bar{1}0]$ direction. The [0001] zone-axis SAED pattern in the inset of Fig. 6b indicates that the α-Fe_2O_3 nanorod is single-crystalline. Fig. 6c shows the enlarged HRTEM image of the region enclosed by a red rectangle in Fig. 6b. The crystal lattice spacing is measured to be 2.51 Å, corresponding to that of the $\{11\bar{2}0\}$ crystal plane in α-Fe_2O_3. Fig. 6d presents the enlarged HRTEM image of a single dislocation in Fig. 6b. The Burgers circuit is drawn to determine the Burgers vector of this dislocation. In Fig. 6d, the red arrow marks a gap between the starting and ending points of the Burgers circuit, from which the Burgers vector $\vec{b}$ is determined to be $\frac{1}{3}[11\bar{2}0]$. This suggests that it is an edge dislocation. The formation of dislocations is beneficial to release residual stress and alleviate lattice distortion during the growth of the α-Fe_2O_3 nanorods.

EELS in STEM mode was used to further analyze the chemical compositions of the α-Fe_2O_3 nanorods. Fig. 7a and b show the typical STEM images of the SnO_2@Fe_2O_3 spheres. The EELS spectra of O–K and Fe $L_{2,3}$ edges are obtained from the region enclosed by a red square in Fig. 7b. Fig. 7c shows the four peaks (A–D) in the O K-edge energy-loss near-edge fine structure (ELNES) of the α-Fe_2O_3 nanorods. Chueh *et al.* found that the intensity of peaks A and B in the O–K edge was closely related to the content of oxygen vacancies in Fe_2O_3.[22] The intensities of peaks A and B in Fig. 7c are weaker than those of α-Fe_2O_3 powder reported in the literature.[23] Studies relate this peak intensity decrease to the presence of oxygen vacancies in α-Fe_2O_3 nanorods.[23–25] Furthermore, by detecting the relative intensity and position of the individual L_3 and L_2 edges of Fe, the ionization state of metal cations can be determined. Fig. 7d shows the EELS spectra of Fe $L_{2,3}$ edges. For the α-Fe_2O_3 nanorods, the intensity ratio $I(L_3)/I(L_2)$ is 4.9, lower than that in a previous report.[23] The L_3 line is situated at 708.15 eV and the spacing between L_3 and L_2 lines is 13.25 eV which is broader than the corresponding value of α-Fe_2O_3 powder.[23] As reported in the previous literature,[23–25] the

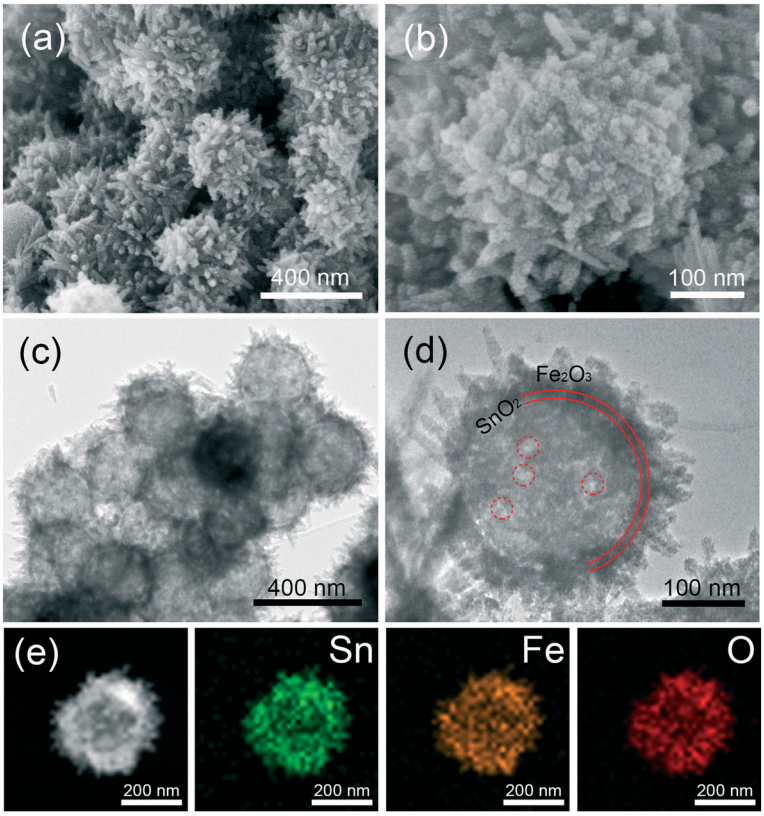

Fig. 5 (a) Typical FESEM images of the SnO_2@α-Fe_2O_3 hollow spheres. (b) Enlarged FESEM image of an individual hollow sphere. (c) BF TEM image of the SnO_2@α-Fe_2O_3 hollow spheres. (d) TEM image of an individual double-shell hollow sphere; red circles indicate the locations of some nanopores. (e) Elemental mapping images of a single SnO_2@α-Fe_2O_3 hollow sphere.

decrease of intensity ratio $I(L_3)/I(L_2)$ and the location of the L_3 line are attributed to the existence of oxygen vacancies in α-Fe_2O_3. Hence, it is a clear indication of the presence of vacancies in our material. It has been proved that the presence of oxygen vacancies could improve the electrochemical performance of metal oxides when used as the anode materials for LIBs.[26,27] Li *et al.* found that the presence of oxygen vacancies in α-Fe_2O_3 nanorods promotes phase change and reduce stress during the insertion/extraction processes of lithium ions, resulting in better cycling stability.[26] In addition, the oxygen vacancies could provide more space for lithium ion storage during battery charging, which would help to improve the specific capacity of α-Fe_2O_3.[28,29] As a result, the increase of the cycling stability and specific capacity of α-Fe_2O_3 also contributes to the whole SnO_2@Fe_2O_3 electrode.

Fig. 8a shows the schematic diagram of the energy band structures for SnO_2 and α-Fe_2O_3. The energy bandgap of SnO_2 and α-Fe_2O_3 is 3.5 eV and 2.2 eV.[30,31] In addition, the Fermi level (E_F) of SnO_2 is higher than that of α-Fe_2O_3. Thus, the electrons transfer from the conduction band of SnO_2 to that of α-Fe_2O_3 across the heterojunction interfaces, and finally their Fermi levels reach an equilibrium.[32,33] Fig. 8b shows the energy band diagram of the SnO_2@Fe_2O_3 heterostructures. The positively-charged SnO_2 and negatively-charged Fe_2O_3 form a built-in electric field because of the electrostatic induction. This electric field could effectively promote electron transfer from Fe_2O_3 to SnO_2 and Li-ion diffusion from SnO_2 to Fe_2O_3 through the heterojunction interfaces, leading to an improvement in the rate performance of the battery.

The specific surface area and pore size of the as-prepared samples were measured by nitrogen adsorption/desorption tests. Fig. 9a shows the type-IV adsorption/desorption isotherms of the three samples with a hysteresis loop, indicating that all the samples possess a mesoporous structure. The pore size distribution curves in Fig. 9b and c illustrate that both SnO_2 and SnO_2@Fe_2O_3 samples have a predominant pore size of 3.9 nm. The total pore volumes of the SiO_2@SnO_2 spheres, SnO_2 hollow spheres and SnO_2@Fe_2O_3 hollow spheres are 0.12, 1.03 and 0.59 $cm^3\ g^{-1}$, respectively. It is found that the total pore volume of the SnO_2@Fe_2O_3 hollow spheres has a smaller value than that of SnO_2 hollow spheres, because some pores on the SnO_2 shells are blocked by the outer Fe_2O_3 nanorods. The Brunauer–Emmett–Teller (BET) surface areas of the SiO_2@SnO_2 spheres, SnO_2 hollow spheres and SnO_2@Fe_2O_3 hollow spheres are calculated to be 15.95, 76.15 and 111.18 $m^2\ g^{-1}$, respectively. The BET surface area of the SnO_2 hollow spheres is larger than that of the SiO_2@SnO_2 spheres, which is ascribed to the internal space of the SnO_2 hollow spheres produced by NaOH etching. The SnO_2@Fe_2O_3 heterostructures have an even larger specific surface area due to the α-Fe_2O_3 nanorods.

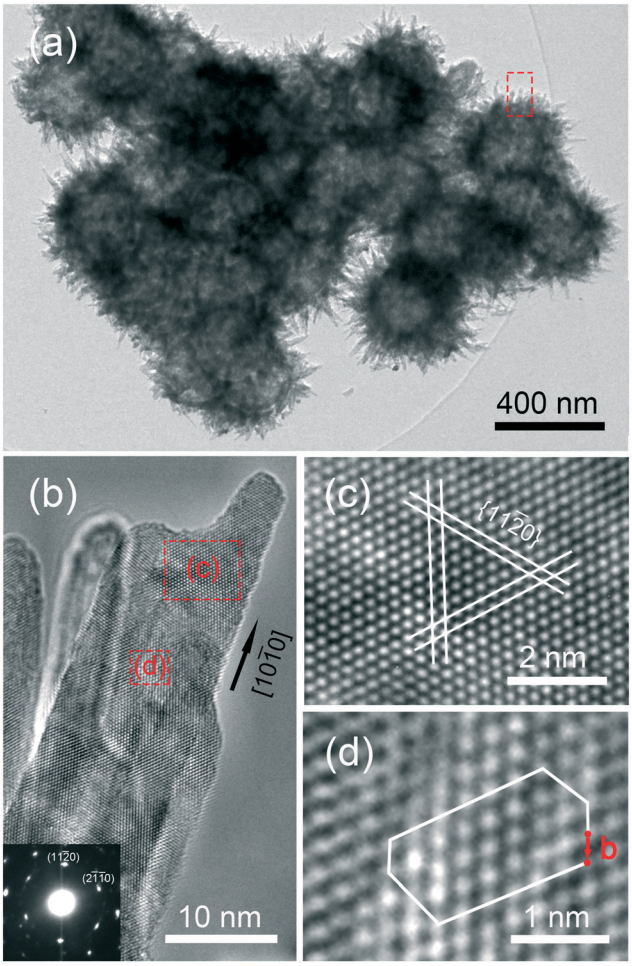

Fig. 6 (a) Typical TEM image of SnO_2@Fe_2O_3 spheres. (b) Typical HRTEM image of SnO_2@Fe_2O_3 spheres. Inset shows the SAED pattern of a single Fe_2O_3 nanorod. (c and d) Enlarged HRTEM images of the regions enclosed by red rectangles in (b).

Owing to their large specific surface area, the SnO_2@Fe_2O_3 heterostructures help to provide more active sites for lithium ion storage, which can greatly enhance the lithium storage capacity.

To evaluate the electrochemical properties, the as-synthesized SiO_2@SnO_2, SnO_2, and SnO_2@Fe_2O_3 are tested as anode materials for LIBs. For the SnO_2@Fe_2O_3 electrode, the electrochemical reactions can be summarized as follows.[15,34]

$$SnO_2 + 4Li^+ + 4e^- \rightarrow 2Li_2O + Sn \quad (1)$$

$$Sn + xLi^+ + xe^- \leftrightarrow Li_xSn\ (0 \le x \le 4.4) \quad (2)$$

$$Fe_2O_3 + 6Li^+ + 6e^- \leftrightarrow 2Fe + 3Li_2O \quad (3)$$

Fig. 10a shows the CV curves of the SnO_2@Fe_2O_3 electrode in the voltage range of 0.01–3.00 V at a scan rate of 0.1 mV s^{-1}. Four distinct reduction peaks at 1.65 V, 1.2 V, 0.51 V and ~0.01 V appear during the first cathodic scan. The reduction peak at 1.65 V might be assigned to the initial insertion of Li ions during the transition from α-Fe_2O_3 to hexagonal $Li_xFe_2O_3$.[15] The peak at 1.2 V is caused by the fact that SnO_2 and Li reacted to form metallic Sn and Li_2O. The peak at 0.51 V is attributed to the redox reactions of Fe_2O_3 with Li producing metallic Fe. Meanwhile, the electrolyte is decomposed to form a solid electrolyte interphase (SEI) layer.[15,34] The presence of a reduction peak (~0.01 V) results from the formation of an Li_xSn alloy. Following the first cycle, the two reduction peaks shift to 1.2 V and 0.76 V, respectively. The subsequent electrochemical process becomes a reversible conversion reaction between metallic Sn, Fe and their oxides. In the process of the anodic scan after the first cycle, the oxidation peaks at 0.57 V and at 1.2 V correspond to the delithiation process in which the Li_xSn alloy is transformed into Sn. The wide peaks at about 1.75 V might be assigned to the reversible oxidation reaction of Fe to Fe_2O_3. Fig. 10b shows the first cycle discharge–charge profiles of the three electrodes. The initial discharge/charge capacity of the SnO_2@Fe_2O_3 composite is 1508 and 1108 mA h g^{-1}, far higher than those of the SnO_2 hollow spheres (1074 and 669 mA h g^{-1}) and SiO_2@SnO_2 sample (801 and 490 mA h g^{-1}), because Fe_2O_3 exhibits higher theoretical specific capacity than SnO_2 and Fe nanoparticles reduced from Fe_2O_3 which can enhance the reversibility of SnO_2.

The cycling performance of the three electrodes was tested at a current density of 100 mA g^{-1} (Fig. 11a). Due to the severe pulverization of electrode materials, the discharge specific capacity of the SnO_2 electrode gradually decreased and maintained only 336 mA h g^{-1} after 190 cycles, resulting in inferior specific capacity and cycling stability. Compared with the SnO_2 electrode, the SiO_2@SnO_2 electrode showed a lower specific capacity of 221 mA h g^{-1} after 190 cycles. By contrast, the reversible specific capacity of the SnO_2@Fe_2O_3 electrode decreased to 464 mA h g^{-1} for the 46th cycle, whereas it increased significantly to 1043 mA h g^{-1} for the 190th cycle. The coulombic efficiency curve of the double-shell SnO_2@Fe_2O_3 hollow spheres is shown in Fig. 11a. For SnO_2, due to the poor reversibility of the SnO_2 conversion reaction ($SnO_2 + 4Li^+ + 4e^- \rightarrow 2Li_2O + Sn$), its initial capacity loss was large and its initial coulombic efficiency was low (62.3%). For SnO_2@Fe_2O_3, due to the improvement of electrochemical reversibility, its initial coulombic efficiency increased up to 73.5%. Through compositing Fe_2O_3 with SnO_2, the initial coulombic efficiency of SnO_2 was improved to some extent. The rate capability of the three electrodes was tested at different current densities of 0.1, 0.2, 0.5, 1 and 2 A g^{-1} and is presented in Fig. 11b. Compared with the other two samples, the SnO_2@Fe_2O_3 electrode exhibited better rate capability with an average discharge capacity of 923.69, 576.67, 460.24, 402.06 and 359.03 mA h g^{-1} at 0.1, 0.2, 0.5, 1 and 2 A g^{-1}, respectively. When the current density returned to 0.1 A g^{-1}, the discharge capacity of the SnO_2@Fe_2O_3 electrode reached 542 mA h g^{-1} after 150 cycles. To investigate the long-term cycling performance, the SnO_2 and SnO_2@Fe_2O_3 electrodes were tested for 1000

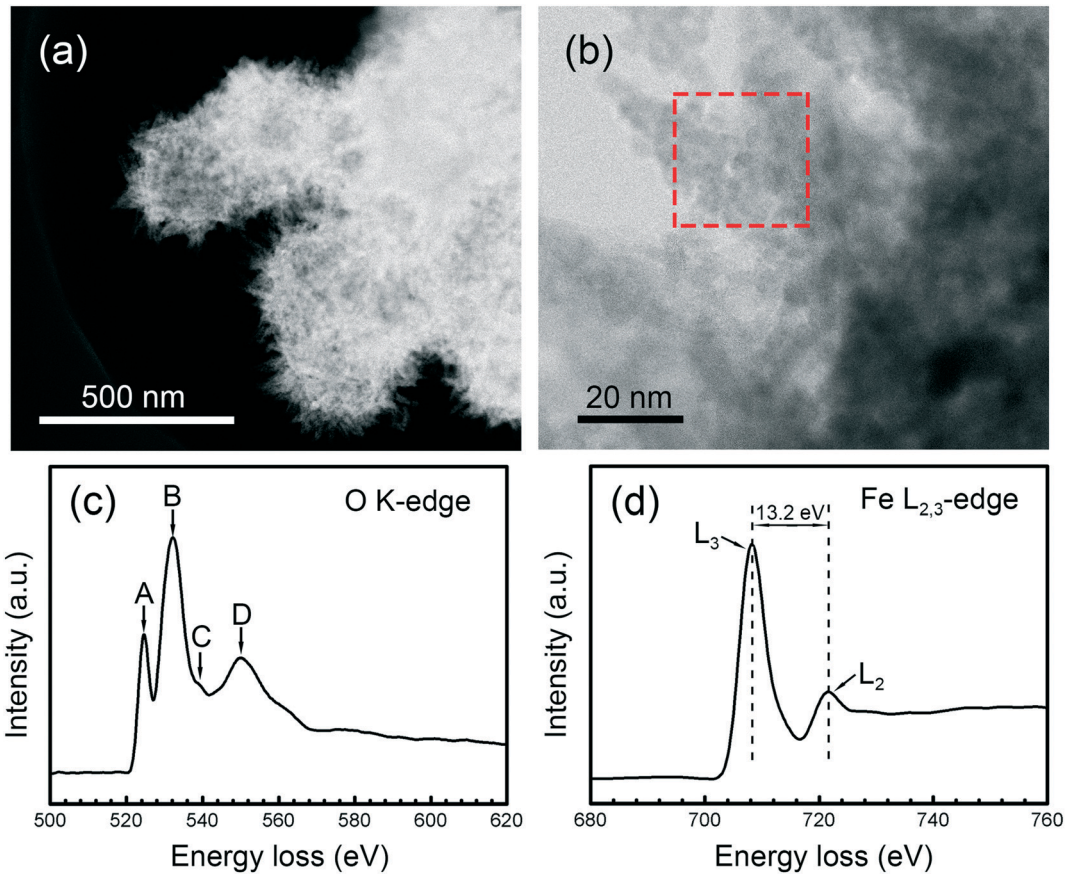

Fig. 7 (a and b) STEM images of the SnO_2@Fe_2O_3 spheres. EELS spectra of oxygen K-edge (c) and Fe $L_{2,3}$-edge (d) obtained from the α-Fe_2O_3 nanorods.

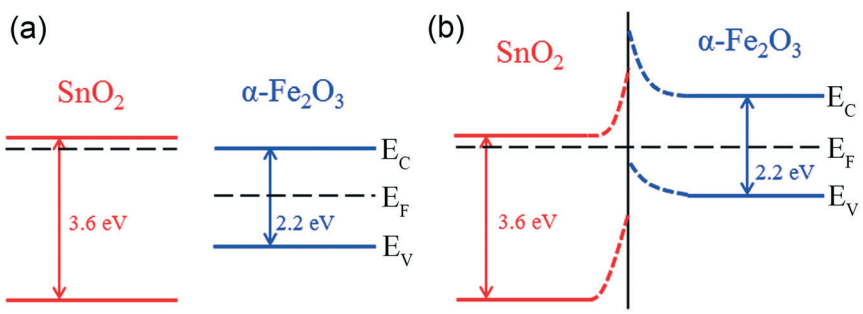

Fig. 8 (a) Schematic diagram of the energy band structures for SnO_2 and α-Fe_2O_3. (b) The energy band diagram of the SnO_2@α-Fe_2O_3 heterostructures. E_C, E_F and E_V stand for conduction band energy, Fermi energy and valence band energy, respectively.

cycles at a high current density of 1000 mA g^{-1} (Fig. 11c). It can be observed that the discharge capacity of SnO_2@Fe_2O_3 decreased to 172.8 mA h g^{-1} after 100 cycles. Then it slowly rose and maintained at a relatively high value of 471.2 mA h g^{-1} after 1000 cycles. Thus, the SnO_2@Fe_2O_3 electrode shows much better cycling performance than SnO_2 at a high current density. Besides, it can be found that the cycle curves of SnO_2@Fe_2O_3 show a similar trend at both high and low current densities. It can be concluded that the SnO_2@Fe_2O_3 electrode exhibits higher specific capacity and better cycling stability than the other two. The high specific capacity of the SnO_2@Fe_2O_3 electrode is attributed to (i) its hierarchical hollow urchin-like structure, (ii) the oxygen vacancies of the α-Fe_2O_3 nanorods and (iii) the SnO_2@Fe_2O_3 heterojunctions. The double-shell SnO_2@Fe_2O_3 hollow spheres with a large specific surface area can provide more active sites during lithium insertion/extraction, which contributes to improving the lithium storage properties. The oxygen vacancies in the α-Fe_2O_3 nanorods provide more space for storage of lithium ions during the charging process. This superior

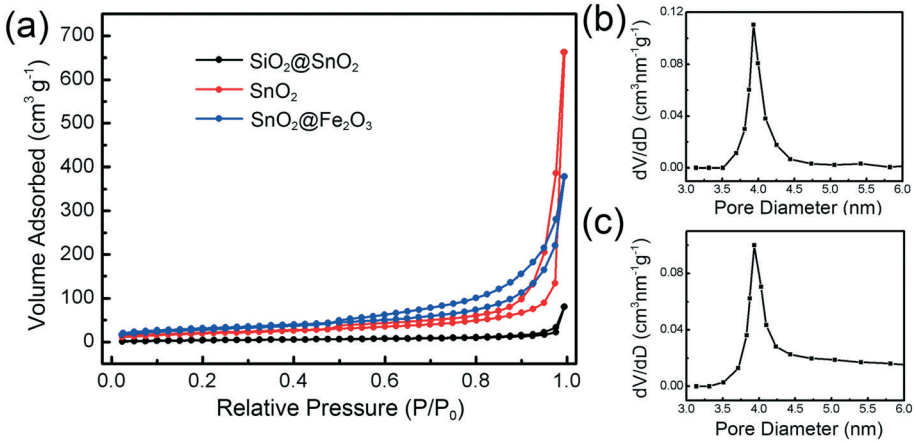

Fig. 9 (a) Nitrogen adsorption/desorption isotherms of the SiO_2@SnO_2 spheres, SnO_2 hollow spheres, and SnO_2@Fe_2O_3 hollow spheres. Pore size distribution curves of the (b) SnO_2 hollow spheres and (c) SnO_2@Fe_2O_3 hollow spheres.

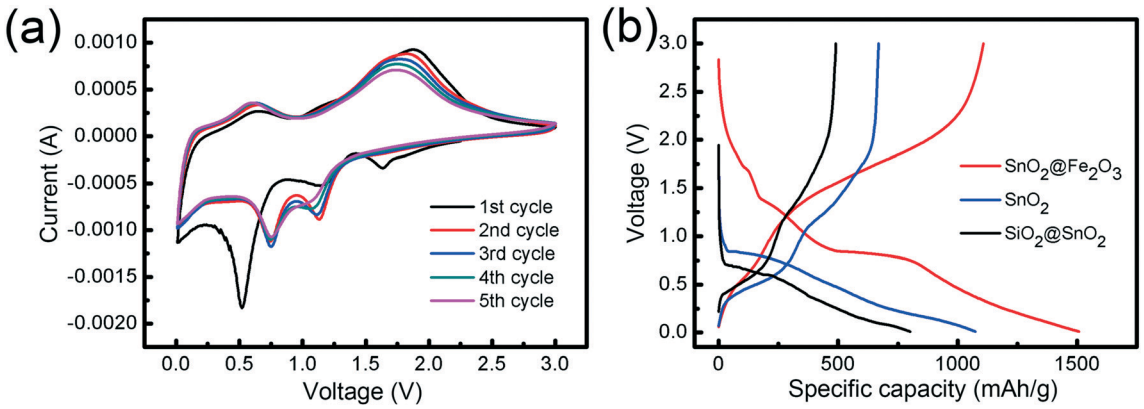

Fig. 10 (a) CV curves of the SnO_2@Fe_2O_3 composite at 0.1 mV s^{-1}. (b) Initial voltage *vs.* capacity curves of SiO_2@SnO_2, SnO_2, and SnO_2@Fe_2O_3 at 100 mA g^{-1}.

electrochemical performance also results from the structure of the SnO_2@Fe_2O_3 heterojunctions, which may be ascribed to the following two points. (1) The structure can inhibit the recombination of electron–hole pairs and facilitate electron transport. (2) The formed built-in electric field will accelerate the electron and lithium ion transfer at the interface of the heterojunctions.

It is worth noting that the discharge capacity decreased before the 46th cycle and then increased significantly. Due to the formation of an organic polymer gel-like layer arising from the incomplete decomposition of the electrolyte, the specific capacity decreased in the initial several cycles. Then the specific capacity increased significantly, which can be attributed to the following reasons. Firstly, the organic polymer gel-like layer could provide excess active sites for lithium storage.[34–37] Secondly, the activation of electrode materials (SnO_2@Fe_2O_3) after several cycles may lead to an improvement of specific capacity.[36] Thirdly, the nanoscaled Fe, reduced from Fe_2O_3, improves the electrochemical kinetic properties of the SnO_2@Fe_2O_3 electrode.[35,38]

Compared with the SiO_2@SnO_2 and SnO_2 samples, the SnO_2@Fe_2O_3 electrode also shows excellent cycling stability even for 190 cycles, because the dense Fe_2O_3 nanorod coating can inhibit the agglomeration of the SnO_2 hollow spheres and mitigate large volume change.

The electrochemical properties of the double-shell SnO_2@Fe_2O_3 hollow spheres and other similar materials are summarized in Table 1 for comparison. Compared with other similar materials, we conclude that the double-shell SnO_2@Fe_2O_3 hollow spheres exhibit superior electrochemical performance.

To explore the electrochemical reaction kinetics of the three samples in detail, EIS measurements were carried out. Fig. 12a presents the EIS spectra of the SiO_2@SnO_2, SnO_2, and SnO_2@Fe_2O_3 electrodes before the first cycle. The EIS spectra consist of a semicircle and a straight line, corresponding to high and low frequency regions, respectively. In the high frequency region, the semicircle diameter of the SnO_2@Fe_2O_3 electrode is smaller than that of SiO_2@SnO_2 and SnO_2, which indicates that SnO_2@Fe_2O_3 has the lowest contact and charge transfer impedance.

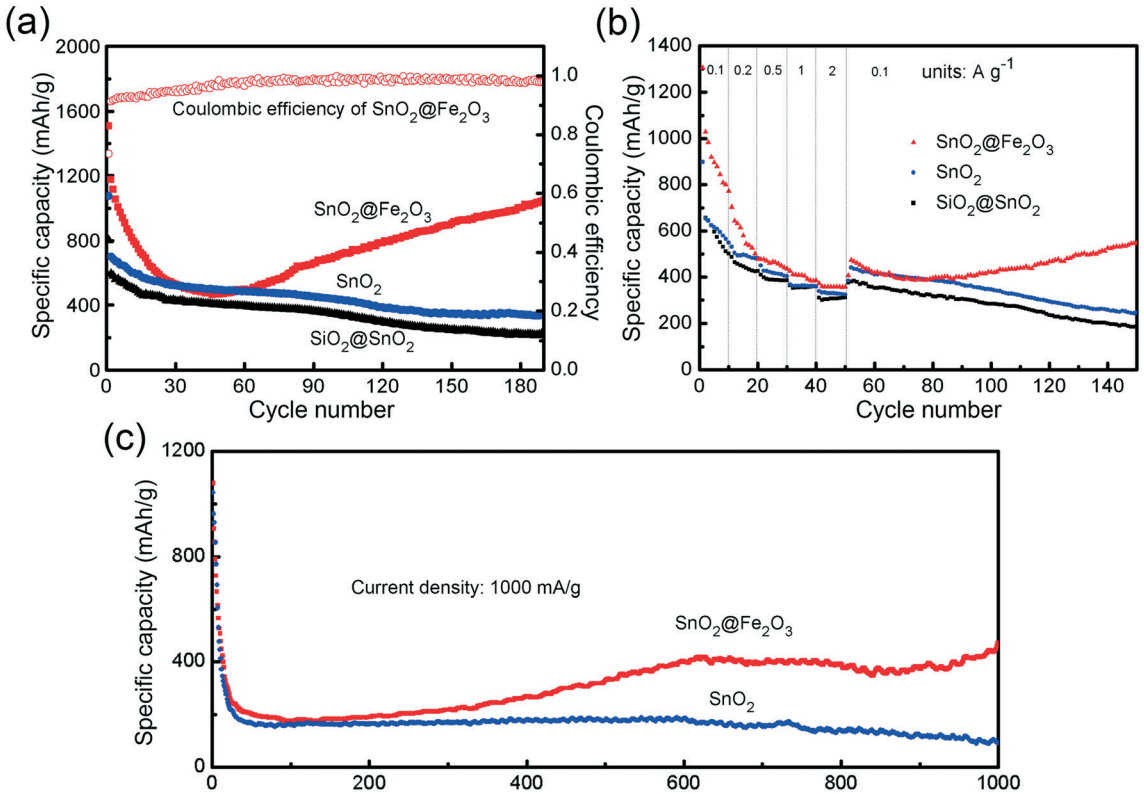

Fig. 11 (a) Comparative cycling performance of SiO_2@SnO_2, SnO_2, and SnO_2@Fe_2O_3 at the same current density of 100 mA g^{-1}. (b) Rate capability of the SnO_2@Fe_2O_3 composite at different current densities. (c) Long-term cycling performance of SnO_2 and the SnO_2@Fe_2O_3 composite at a high current density of 1000 mA g^{-1}.

Table 1 A comparison of the electrochemical properties of the metal oxide based anode materials

Sample	Current density (mA g^{-1})	Cycle number	Specific capacity after cycling (mA h g^{-1})	Ref.
SnO_2–Fe_2O_3@RGO	200	100	830	39
Hierarchical SnO_2/Fe_2O_3 hollow spheres	500	100	454.7	16
SnO_2–Fe_2O_3–C hollow nanospheres	200	100	1100	17
Hierarchical SnO_2 nanorods/Fe_2O_3 hexahedra	100	100	1022	38
Core–shell α-Fe_2O_3/SnO_2	100	30	341	40
α-Fe_2O_3 porous microrods	100	100	733	41
Terminal hollowed Fe_2O_3@SnO_2	200	100	570.7	42
Porous SnO_2–Fe_2O_3 nanocubes	200	50	567.5	14
Carbon-coated SnO_2@carbon nanofibers	100	50	492	43
Double-shell SnO_2@Fe_2O_3 hollow spheres	100	190	1043	This work

Fig. 12b presents the EIS spectra of the SnO_2@Fe_2O_3 electrode before the first cycle and after the 190th cycle. It can be found that the semicircle diameter of the SnO_2@Fe_2O_3 electrode after cycling is smaller than that of the electrode before cycling, proving that the SnO_2@Fe_2O_3 electrode after cycling exhibits faster charge transfer. The EIS analyses demonstrate that the SnO_2@Fe_2O_3 hollow structure shortens the diffusion path of lithium ions. Coupled with the acceleration effect of the heterojunction structure, it can greatly promote charge transfer.

To elucidate the structural stability of the double-shell SnO_2@Fe_2O_3 hollow spheres, the TEM of the electrode materials (after the 190th cycle at a current rate of 100 mA g^{-1}) was carried out. After repeated Li^+ insertion/extraction, we still observe the SnO_2@Fe_2O_3 composite keeping its urchin-like structure (Fig. 13a). TEM reveals that the hollow urchin-like heterostructures exhibit superior structural stability, proving that the structure can effectively buffer volume expansion and alleviate strain. In Fig. 13b, a single nanoparticle with a size of 4 nm is found on the surface of the SnO_2 hollow sphere (now an Li_xSn shell). The lattice spacing of the nanoparticle is 2.05 Å, which corresponds to that of Fe (110) planes. The Fe nanoparticle is thought to be reduced from Fe_2O_3, which can increase the overall conductivity of the electrodes, in agreement with the EIS results (Fig. 12b). Thus, the charge transfer kinetics is improved, leading to an increment of the capacity in the following cycles.[35]

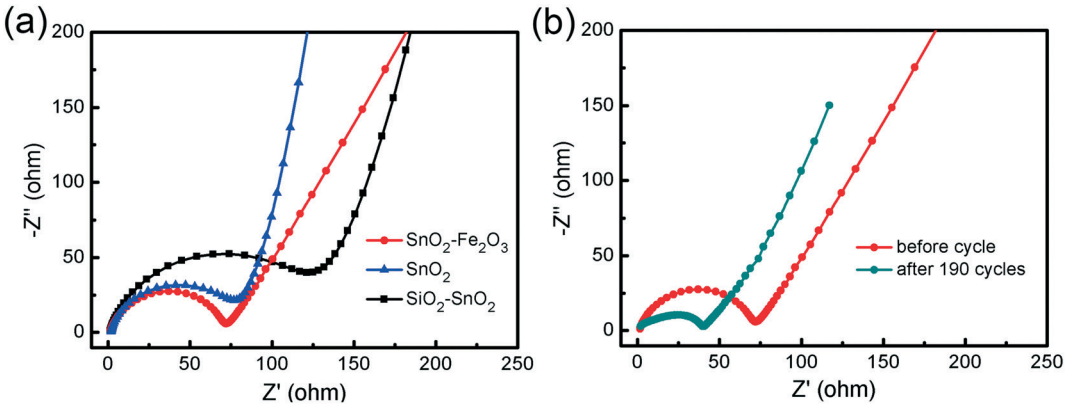

Fig. 12 (a) EIS spectra of the SiO_2@SnO_2, SnO_2, and SnO_2@Fe_2O_3 electrodes before the first cycle. (b) EIS spectra of the SnO_2@Fe_2O_3 electrode before the first cycle and after the 190th cycle.

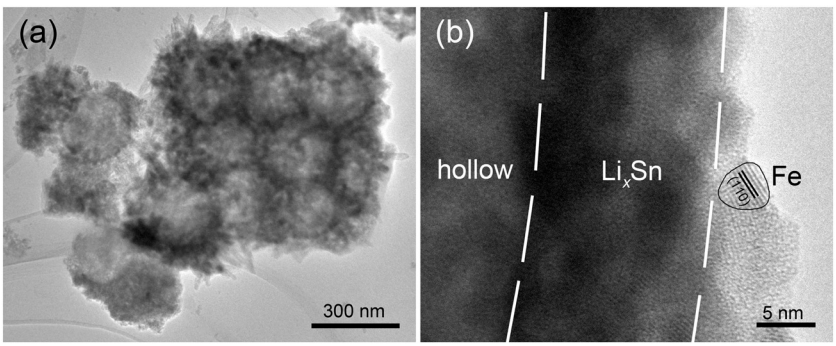

Fig. 13 BF TEM image (a) and HRTEM image (b) of the SnO_2@Fe_2O_3 electrode after 190 cycles at a current density of 100 mA g^{-1}.

4. Conclusions

In summary, double-shell SnO_2@Fe_2O_3 hollow spheres with enhanced performance as lithium ion battery anodes have been synthesized by a template-based method. It turns out that the SnO_2@Fe_2O_3 composite exhibits higher specific capacity, better rate capability, and greatly enhanced cycling stability compared to SiO_2@SnO_2 and SnO_2 electrodes. The reversible capacity of the SnO_2@Fe_2O_3 electrode is up to 1043 mA h g^{-1} after 190 cycles at a current density of 100 mA g^{-1}. The superior lithium storage capacity and cycling stability originate from the unique hierarchical hollow urchin-like structure, the SnO_2@Fe_2O_3 heterojunctions and the oxygen vacancies in the α-Fe_2O_3 nanorods. Based on the experimental results, it is obvious that this novel urchin-like hollow structure can be implemented to inhibit the agglomeration of nanomaterials and alleviate volume expansion during the processes of lithium insertion/extraction. This work demonstrates that such double-shell SnO_2@Fe_2O_3 hollow spheres provide a new horizon for constructing high performance anode materials for LIBs.

Conflicts of interest

There are no conflicts to declare.

Acknowledgements

Y. Q. Wang would like to thank the financial support from the High-end Foreign Experts Recruitment Programs (Grant No.: GDW20173500154, GDW20163500110), the Shandong Province "Double-Hundred Talent Plan" (Grant No.: WST2018006), the Shandong Province High-end Foreign Experts Recruitment Program, the Shandong Province Taishan Scholar Program, the Qingdao International Center for Semiconductor Photoelectric Nanomaterials, and the Shandong Provincial University Key Laboratory of Optoelectrical Material Physics and Devices. J. Y. Zhong would like to thank the start funding support from Qingdao University (DC1900003208) and the Innovative Teaching Laboratory Research Project of Qingdao University.

References

1 J. M. Tarascon and M. Armand, *Nature*, 2001, **414**, 359–367.
2 G. Zubi, R. Dufo-Lopez, M. Carvalho and G. Pasaoglu, *Renewable Sustainable Energy Rev.*, 2018, **89**, 292–308.
3 M. B. Zheng, H. Tang, L. L. Li, Q. Hu, L. Zhang, H. G. Xue and H. Pang, *Adv. Sci.*, 2018, **5**, 1700592.

4 L. M. Zhou, K. Zhang, Z. Hu, Z. L. Tao, L. Q. Mai, Y. M. Kang, S. L. Chou and J. Chen, *Adv. Energy Mater.*, 2018, **8**, 1701415.
5 B. Liu, X. Y. Zhao, Y. Tian, D. Zhao, C. W. Hu and M. H. Cao, *Phys. Chem. Chem. Phys.*, 2013, **15**, 8831–8837.
6 Z. F. Ma and T. B. Zhao, *Electrochim. Acta*, 2016, **201**, 165–171.
7 Y. Zhao, X. F. Li, B. Yan, D. B. Xiong, D. J. Li, S. Lawes and X. L. Sun, *Adv. Energy Mater.*, 2016, **6**, 1502175.
8 L. Zhang, H. B. Wu and X. W. Lou, *Adv. Energy Mater.*, 2014, **4**, 1300958.
9 M. S. Faramarzi, A. Abnavi, S. Ghasemi and Z. Sanaee, *Mater. Res. Express*, 2018, **5**, 065040.
10 R. Mao, H. Guo, D. X. Tian, D. P. Zhao, X. J. Yang, S. X. Wang and J. Chen, *Mater. Res. Bull.*, 2013, **48**, 1518–1522.
11 G. D. Park, J. K. Lee and Y. C. Kang, *Adv. Funct. Mater.*, 2017, **27**, 1603399.
12 T. M. Zhang, J. Z. Zheng, Z. Q. Liang, B. Zhao, H. J. Zeng, W. Guo, L. Zhao, Y. H. Sun, I. Abdulhalim and L. Jiang, *Electrochim. Acta*, 2019, **306**, 151–158.
13 M. V. Reddy, T. Yu, C. H. Sow, Z. X. Shen, C. T. Lim, G. V. S. Rao and B. V. R. Chowdari, *Adv. Funct. Mater.*, 2007, **17**, 2792–2799.
14 Y. Yan, F. H. Du, X. P. Shen, Z. Y. Ji, H. Zhou and G. X. Zhu, *Dalton Trans.*, 2014, **43**, 17544–17550.
15 Y. Zeng, J. Z. Luo, Y. Z. Wang, L. Qiao, B. Zou and W. T. Zheng, *Nanoscale*, 2017, **9**, 17576–17584.
16 R. C. Jin, Y. S. Guan, H. Liu, J. H. Zhou and G. Chen, *ChemPlusChem*, 2014, **79**, 1643–1648.
17 J. Choi, W. S. Kim and S. H. Hong, *Nanoscale*, 2018, **10**, 4370–4376.
18 W. Stöber, A. Fink and E. Bohn, *J. Colloid Interface Sci.*, 1968, **26**, 62–69.
19 H. Zhang, A. J. Xie, C. P. Wang, H. S. Wang, Y. H. Shen and X. Y. Tian, *J. Mater. Chem. A*, 2013, **1**, 8547–8552.
20 M. S. Moreno, R. F. Egerton and P. A. Midgley, *Phys. Rev. B: Condens. Matter Mater. Phys.*, 2004, **69**, 233304.
21 F. de la Pena, M. H. Berger, J. F. Hochepied, F. Dynys, O. Stephan and M. Walls, *Ultramicroscopy*, 2011, **111**, 169–176.
22 Y. L. Chueh, M. W. Lai, J. Q. Liang, L. J. Chou and Z. L. Wang, *Adv. Funct. Mater.*, 2006, **16**, 2243–2251.
23 H. L. Feng, Y. Q. Wang, C. Wang, F. Y. Diao, W. H. Zhu, P. Mu, L. Yuan, G. W. Zhou and F. Rosei, *Nanotechnology*, 2016, **27**, 295703.
24 C. Wang, Y. Q. Wang, X. H. Liu, H. W. Yang, J. R. Sun, L. Yuan, G. W. Zhou and F. Rosei, *Nanotechnology*, 2016, **27**, 035702.
25 R. S. Cai, L. Shang, X. H. Liu, Y. Q. Wang, L. Yuan and G. W. Zhou, *Chin. Phys. B*, 2013, **22**, 107401.
26 N. Li, K. Du, G. Liu, Y. P. Xie, G. M. Zhou, J. Zhu, F. Li and H. M. Cheng, *J. Mater. Chem. A*, 2013, **1**, 1536–1539.
27 H. Song, T. G. Jeong, Y. H. Moon, H. H. Chun, K. Y. Chung, H. S. Kim, B. W. Cho and Y. T. Kim, *Sci. Rep.*, 2014, **4**, 4350.
28 Y. Xu, M. Zhou, X. Wang, C. L. Wang, L. Y. Liang, F. B. Grote, M. H. Wu, Y. Mi and Y. Lei, *Angew. Chem., Int. Ed.*, 2015, **54**, 8768–8771.
29 T. Y. Yang, H. Y. Kang, U. Sim, Y. J. Lee, J. H. Lee, B. Koo, K. T. Nam and Y. C. Joo, *Phys. Chem. Chem. Phys.*, 2013, **15**, 2117–2124.
30 Q. X. Yu, J. H. Zhu, Z. Y. Xu and X. T. Huang, *Sens. Actuators, B*, 2015, **213**, 27–34.
31 J. Zhang, X. H. Liu, L. W. Wang, T. L. Yang, X. Z. Guo, S. H. Wu, S. R. Wang and S. M. Zhang, *Nanotechnology*, 2011, **22**, 185501.
32 L. X. Zheng, S. C. Han, H. Liu, P. P. Yu and X. S. Fang, *Small*, 2016, **12**, 1527–1536.
33 M. T. Greiner, M. G. Helander, W. M. Tang, Z. B. Wang, J. Qiu and Z. H. Lu, *Nat. Mater.*, 2012, **11**, 76–81.
34 T. Li, T. Xin, Y. H. Ding, J. J. Zou, H. Q. Liu, B. Liu and Y. Q. Wang, *J. Solid State Electrochem.*, 2019, **23**, 379–387.
35 J. S. Luo, J. L. Liu, Z. Y. Zeng, C. F. Ng, L. J. Ma, H. Zhang, J. Y. Lin, Z. X. Shen and H. J. Fan, *Nano Lett.*, 2013, **13**, 6136–6143.
36 Z. Y. Wang, D. Y. Luan, S. Madhavi, Y. Hu and X. W. Lou, *Energy Environ. Sci.*, 2012, **5**, 5252–5256.
37 W. J. Yu, P. X. Hou, F. Li and C. Liu, *J. Mater. Chem.*, 2012, **22**, 13756–13763.
38 T. Xin, F. Y. Diao, C. Li, H. L. Feng, G. J. Liu, J. J. Zou, Y. H. Ding, B. Liu and Y. Q. Wang, *Mater. Res. Bull.*, 2018, **99**, 196–203.
39 B. Zhao, Y. T. Xu, S. Y. Huang, K. Zhang, M. M. F. Yuen, J. B. Xu, X. Z. Fu, R. Sun and C. P. Wong, *Electrochim. Acta*, 2016, **202**, 186–196.
40 Y. F. Li, Y. J. Hu, H. Jiang, X. Y. Hou and C. Z. Li, *CrystEngComm*, 2013, **15**, 6715–6721.
41 S. W. Yao, Z. Q. Shi and X. X. Zhang, *J. Alloys Compd.*, 2019, **794**, 333–340.
42 F. Li, G. E. Luo, J. F. Yu, W. J. Huang, D. H. Xu, W. Y. Chen, X. Y. Huang, S. Y. Yang, Y. P. Fang and X. Y. Yu, *J. Alloys Compd.*, 2019, **773**, 778–787.
43 W. Wang, Y. H. Liang, Y. F. Kang, L. S. Liu, Z. W. Xu, X. Tian, W. Mai, H. J. Fu, H. M. Lv, K. Y. Teng, X. N. Jiao and F. Y. Li, *Mater. Chem. Phys.*, 2019, **223**, 762–770.